DOI: 10.61782/fa.2025.0761

FORUM ACUSTICUM
EURONOISE 2025

ROTOR NOISE CONTROL USING COAXIAL CO-ROTATING ROTORS.

Charles E. Tinney[1†] **Yingjun Zhao-Dubuc**[1] **John Valdez**[1]
[1] Applied Research Laboratories, University of Texas at Austin, Austin, Texas, USA
https://www.arlut.utexas.edu/gdl

ABSTRACT

The development of a low-noise rotor blade has received considerable attention in recent years due to emerging interests in electric vertical take-off and landing (eVTOL) vehicles. One of the most impact-full methods for reducing the acoustic footprint from multirotor platforms is by augmenting the angular phase between neighboring rotors so that sound waves interfere either constructively or destructively for an observer in the far-field. For stacked, co-rotating rotors operating in hover, this form of noise control has been shown to augment rotor performance, thereby providing a trade-space between changes in noise, versus changes in performance. Here we evaluate the same trade-space using a combination of low-order analysis methods capable of filtering out the most energetic waveforms that make up the sound field of this rotor. This combines the conventional form of the proper orthogonal decomposition (POD) with vold-kalman filters (VKF) to filter structures in both space and time, respectively. The findings show that for an observer located below the rotor disk plane, sound pressure levels corresponding to the first few blade pass frequency harmonics can be reduced by as much as 4 dB with only moderate losses in hover efficiency.

Keywords: *Drone noise, eVTOL, UAM, AAM, co-rotating rotors, rotor noise control, proper orthogonal decomposition, Vold-Kalman filters.*

**Corresponding author*: ✉ *charles.tinney@arlut.utexas.edu.*

1. BACKGROUND

Most studies concerned with the acoustics of multirotor platforms focus on side-by-side configurations with or without synchrophase control. The coaxial (stacked), co-rotating rotor is another multirotor configuration that, unlike the traditional side-by-side setup, ha an acute sensitivity to both performance and acoustics on account of changes to rotor operating conditions. As such, the co-rotating offers a much more promising approach for controlling rotor noise through the constructive and destructive interference (CDI) of sound waves generated by neighboring rotors. These sources of noise are the result of thickness noise and blade loading noise, which are impulsive (unlike rotor broadband noise), and are the key drivers of community annoyance. In 2018, a number of initiates began at the Applied Research Laboratories, The University of Texas at Austin (ARL:UT) to study this trade-space with key findings being published in a number of conference papers [1, 2] and journal articles [2–4]. This paper serves to review the highlights of these findings, while providing new results for the interested reader. Other efforts to characterize the hover performance and acoustics of stacked rotors can be found in the literature [5, 6].

2. HARDWARE AND SETUP

Measurements were performed in the Gas Dynamics Laboratory (GDL) at ARL:UT near standard sea level conditions ($p_\infty = 14.7$ psia (103,325 Pa), $T_\infty = 526$ R (292 K), $\rho = 2.34 \times 10^{-}3$ slug/ft^3 and $a_\infty = 1.126 \times 10^3$ ft/s). A description of the GDL can be found here: `https://www.arlut.utexas.edu/gdl/` and is a 24 ft tall acoustically treated facility enclosing $\dot{V} = 30,100$ ft^3 of open air space over 1,500 ft^2 of floor space. The performance and acoustics of various rotor platforms covering

Table 1. Definitions for rotor index angle ϕ [deg] and rotor lead/lag φ [deg].

j	1	2	3	4	5	6
ϕ_j [deg]	12	30	48	66	84	102
φ_j [deg]	12	30	48	66	84	-78
k	7	8	9	10	11	
ϕ_j [deg]	120	138	156	174	192	
φ_j [deg]	-60	-42	-24	-6	12	

a range of scales have been tested over the years at the GDL, [7,8]. For now, we will concentrate on a stacked co-rotating configuration using model 18×5.5 MR-P blades ($D = 18$ in.) manufactured by APC Propellers. These blade shapes are highly twisted and are inverted with the rotor disk plane elevated 105 inches from the laboratory floor so that the thrust vector points down. This equates to a distance of sixteen rotor diameters between the rotor disk plane and the virtual floor (ceiling) to reduce ground effects.

The upper blade assembly was designed so that changes to both rotor index angle (angle between upper and lower rotors ranging between $\phi_1 = 12$ deg and $\phi_{11} = 192$ deg with $\delta\phi = 18$ deg increments) and stacking distances between rotors could be tightly controlled. Table 1 lists the notation used to identify the differences between index angle (ϕ_j) and lead/lag angle (φ_j) where φ is positive when the upper rotor is leading the lower rotor in the direction of rotation. The third variable of interest is rotor rotation speed, which varied from $\omega = 50$ rotations per second (RPS) to 90 rps, in 10 rps increments. Only the $\omega = 90$ rps and $\delta z/D = 0.061$ condition will be evaluated here and corresponds to a blade chord Reynolds number at $r = 0.75R$ of $\mathrm{Re}_{c75} = 1.9 \times 10^5$ and a blade tip Mach number valued at 0.38. An illustration of the upper assembly with rotor blades is shown in Fig. 1a.

3. ROTOR PERFORMANCE

Several instruments were used to understand the mechanisms governing the trade-space between hover performance and acoustics, and the effect of synchrophasing on rotor noise control. The first of these was a Futek model MBA500 bi-axial load cell for measuring axial thrust and torque with reported errors of 0.125 lbf and 0.125 in-lbf, respectively. Thrust coefficient $C_T = F_z/(\rho A \Omega^2 R^2)$, torque coefficient $C_\tau = \tau/\rho A_d (\Omega R)^2 R$, and rotor figure

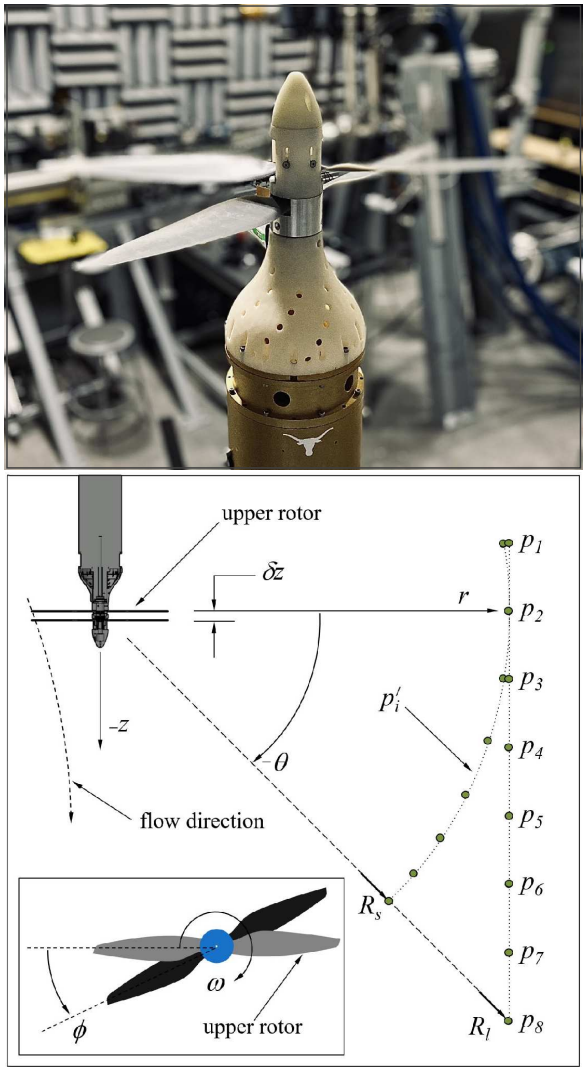

Figure 1. a) The coaxial, co-rotating rotor used by Tinney and Valdez [1] with APC propeller models 18×5.5 MR(P) b) Orientation of rotor test stand with coordinate system.

of merit $FM = C_T^{3/2}/\sqrt{2}/C_\tau$, were calculated for each test case where $R = D/2$ is rotor radius, $A = \pi D^2/4$ is rotor disk area and Ω is motor rotation speed in rad/s ($\Omega = 2\pi\omega$). In Fig. 2a, thrust coefficient and torque coefficient are reported for the 90 rps rotor speed and with systematic changes to rotor index angle. Rotor efficiency is reported in Fig.2b and is typical of rotors of this scale [7]. The findings demonstrate the key features of the stacked, co-rotating rotor. The first is that changes in rotor index

angle have a profound impact on hover performance and that the optimum hover performance is achieved when the upper rotor lags the lower rotor. This occurs for this rotor configuration around $\varphi = -30$ deg.

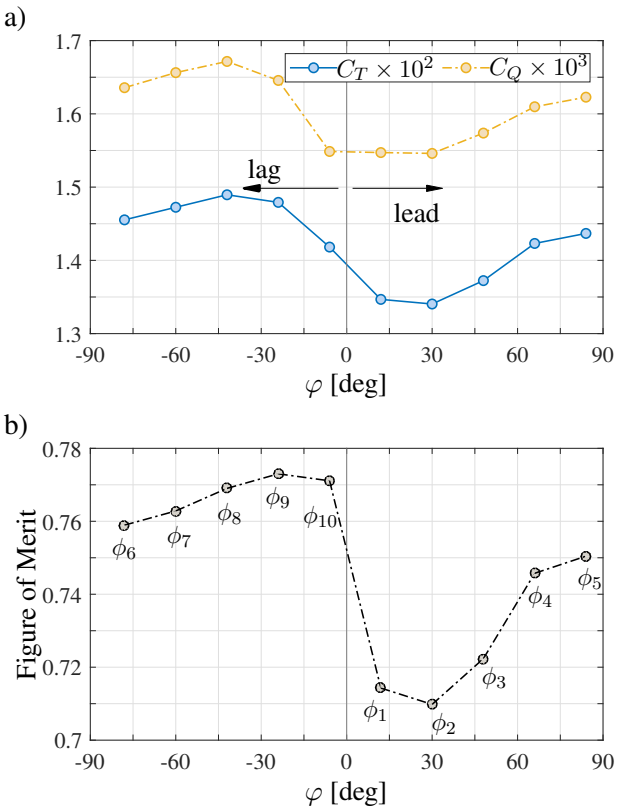

Figure 2. a) Thrust coefficient, torque coefficient, and b) rotor figure of merit at 90 rps rotor speed.

4. ROTOR WAKE AND SLIPSTREAM

A single camera PIV system mounted to a two-stage linear traverse was then used to measure the wake and slipstream boundaries generated by the stacked rotor [3]. The measurement window was oriented to capture vortices from both the upper and lower blades including provisions for wander. The principal components of the PIV system comprised a Nd-YAG laser, a single 2M pixel CCD camera operating at sample rate of 7 Hz (double frame mode), as well as a PIVTEC 14 Laskin nozzle seeder for generating 0.1 to 1.0μm size olive oil particles. A total of 250 statistically independent image pairs were captured for each of the 37 wake ages ($0° \leq \psi \leq 360°$ deg in increments of $\Delta\psi = 10$ deg) and all eleven index angles thereby resulting in a total of 101,750 image pairs that were converted to vector maps using DaVis v.10.1. The location of the slipstream boundary was identified using the Γ_1-method to correct for vortex jitter. Numerous reviews on both integral-based and divergence-based schemes for characterizing vortex jitter are provided by Mula et al. [9] and the references therein.

A sample result from the PIV system is shown in Fig. 3 for the stacked rotor operating at 90 rps with $\delta z/D = 0.061$ and $\phi_1 = 12$ deg. At each wake age, small grey symbols identify the instantaneous locations of jittering vortices from all snapshots, followed by the average value (large color symbols). Lines are drawn connecting the trajectory of vortices generated by the upper and lower rotors with increasing wake age. The full PIV database is then compiled to identify the flow mechanisms responsible for effecting changes to hover performance. This is accomplished by evaluating the miss distance between the upper rotor vortices with the lower rotor blade, which is plotted in Fig. 4. Here, the solid symbols are from direct measurements while open symbols are extrapolated from trajectories of the vortex using the last known measurements from that index angle. The findings demonstrate that for a given rotor speed, index angle and stacking distance of the co-rotating rotor, thrust is maximum when the tip vortex generated by the upper rotor grazes the low pressure side of the lower rotor.

5. ROTOR ACOUSTICS

The last of the instruments used for this study was a line array of eight 1/2-inch free-field microphones (G.R.A.S. model 46AE with matching preamplifiers) positioned three rotor diameters from the hub with equal spacings of $z_i/D = 0.5$, and with the second microphone aligned with the rotor disk plane as shown in Fig. 1b. Remaining sensors were then biased towards locations below the rotor resulting in an acoustic corridor between $\theta_1 = 9.5°$ (above the rotor) and $\theta_8 = -45°$ (below the rotor). Microphone signals were sampled uninterrupted for 20.48 seconds at a rate of $f_s = 40$ kHz using 24 bit accurate A/D converters. Acoustic waveforms were then propagated using $p \propto 1/r$ decay to a virtual arc array located three rotor diameters from the hub and identified by p' in Fig. 1b. Ensemble averaged sound pressure spectrum levels (SPSL, Re: 20μPa) are computed using a Hanning window with 75% overlap and a spectral resolution of $f_s/N = \delta f = 2.0345$ Hz. No corrections for atmospheric absorption or human ear effects are employed. Albeit, precautions should be taken when conducting acous-

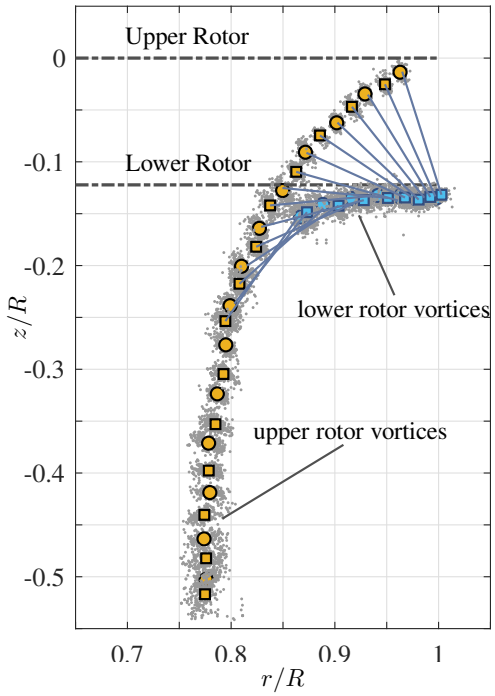

Figure 3. Average vortex locations from the upper and lower rotors of the stacked rotor operating at 90 rps with $\delta z/D = 0.061$ and $\phi_1 = 12$ deg.

tic and performance measurements in enclosed facilities which warrant some discussion.

5.1 Gauging Facility Enclosure Effects

Determining whether facility effects are corrupting one's measurements continues to be a contentious topic of discussion at conferences and workshops. While there is no unified framework for gauging these effects, some simple exercises can be performed during testing and are listed as follows:

i ***Facility time-scale:*** The first of these seeks to estimate the time required for the rotor to fully digest the volume of air enclosed by the facility. This was proposed by [8] and was motivated by concerns over recirculation effects [10]. This facility time-scale is determined by $t_v = \dot{V}/(Av_i)$ and uses rotor inflow $v_i = \lambda\Omega R$ and inflow ratio $\lambda_i = \sqrt{C_T/2}$ as inputs. For the highest thrust generating condition of this stacked rotor, the facility time scale is valued at $t_v = 465$ [s] and is sufficiently large for enclosure effects to be considered negligible.

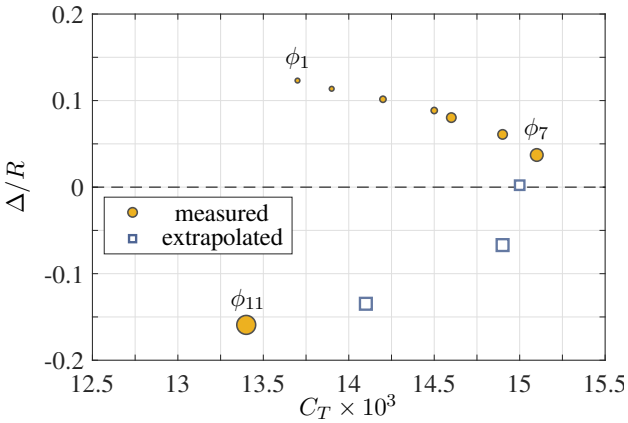

Figure 4. Miss-distance (Δ) between the upper rotor tip vortex and the lower rotor centerline versus thrust coefficient for ω_5 and δz_1. Symbol size increases with increasing index angle ϕ_k.

ii ***Spherical decay:*** If measurements are in the acoustic field and the source is compact, then pressure amplitudes should follow the $p \propto 1/r$ decay law. A simple check for this was performed using the isolated rotor spinning at $\omega = 90$ rps and by traversing a single microphone radially along the rotor disk plane between $1.0 \leq r/D \leq 8.0$. The findings are shown in Fig. 5 where the onset of spherical decay appears around $r/D \sim 2.5$ from the hub. Errors, relative to the spherical decay law, are 1.17 dB for $r/D \geq 2.5$, that then reduce to 1.03 dB for $r/D \geq 3.0$.

iii ***Isolating motor noise:*** Most drone scale rotor measurements are powered using outrunner type brushless DC motors, which are notoriously loud. The source of motor noise is well known and is caused by the first few structural modes of the motor casing [11]. Most motor noise falls into the same frequency bands where rotor broadband noise is prevalent. As such, SPSL provides an easy metric for gauging whether facility or motor noise tones are leaking into the rotor noise measurements. This is evaluated using the isolated rotor operating at 90 rps and is shown in Fig. 6 where $f_b = N_b \cdot \omega$ is the blade-pass frequency. Noise from the motor appears in some of the higher frequency tones (above $10 f_b$). The shapes and amplitudes are what one might expect for rotors of this scale.

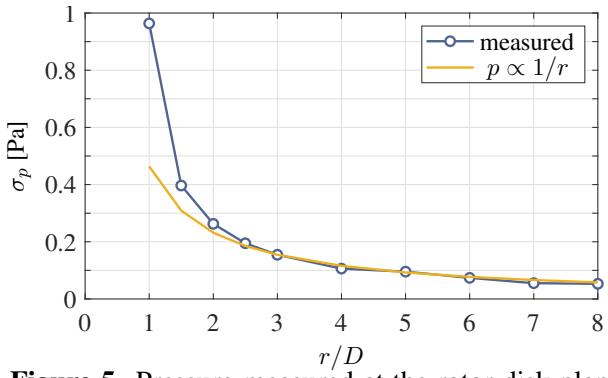

Figure 5. Pressure measured at the rotor disk plane compared with the $1/r$ decay for the isolated rotor at 90 rps.

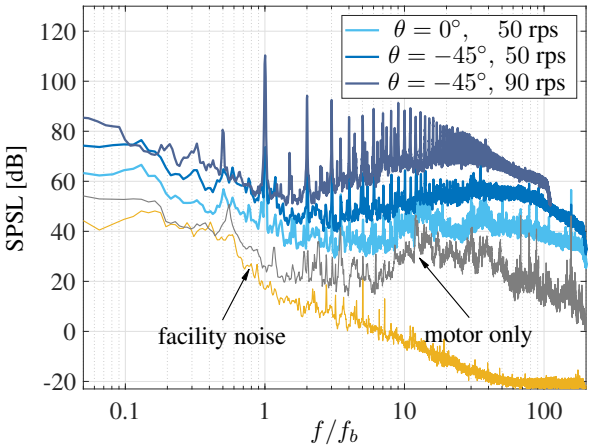

Figure 6. Background noise relative to the isolated two-blade rotor. Subsequent spectra are shifted upwards by 10 dB.

5.2 Constructive and Destructive Interference

A known feature of synchrophased rotors is the constructive and destructive interference of sound waves generated by neighboring blades and their effect on the far-field noise. This is not limited to co-rotating stacked rotors and is a common discussion point for studies involving multi-rotor platforms operating numerous motors independently without phase-synchronized control. That is, tones appear intermittently, due to nonlinear coupling between neighboring rotors and was shown early on using wavelet spectra of Tinney and Sirohi [12]. A simple demonstration of this is shown in Fig. 7 using two acoustic pressure time series from an isolated rotor (some filtering of the data has been performed to improve clarity). The pressure waveforms are identical and are used to generate a new waveform $\hat{p}(\tau) = p(t) + p(t+\tau)$ by retarding the same measured waveform using $\tau = \phi_k/\omega \cdot 360$ as the retarded time. Calculating this effect over all rotor index angles ϕ_k demonstrates the change from constructive interference to destructive interference.

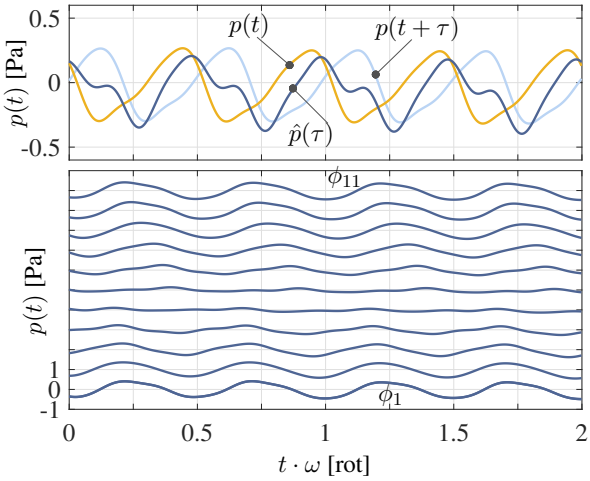

Figure 7. Top: Linear superposition of an acoustic pressure time series with its retarded time. Bottom: Comparison between estimates and measurements of acoustic pressure time series for ω_5 and δz_1. Adapted from Tinney and Valdez [1].

5.3 Analysis methods.

Data reduction techniques play a pivotal role in separating out features responsible for governing the bulk physics of a system. To this end, a number of techniques have been proposed that combine various forms of the POD (conventional, spectral, gappy) with Vold Kalman filters, to distill structure from unsteady stationary signals. In what follows, the outline of one such approach is described and is leveraged to flush out the mechanisms responsible for generating the abundance of noise generated by synchrophased stacked rotors. The process first decomposes spatially evolving acoustic waveforms using the conventional form of the POD, followed by filtering of the first few rotor harmonics using Vold Kalman filters.

5.3.1 *Conventional POD*

The simplest form of Lumley's POD is one where the kernel comprises a covariance matrix that forms from the inner product of one of two variables that make up the vector

space. In this case, the two variables stretch over space (θ) and time (t), so that

$$R(\theta,\theta') = \sum_t p(\theta,t)p^*(\theta',t) \tag{1}$$

which is self-adjoint: $\det([R_{\theta\theta'}]^{-1}) = 0$. An eigenvalue problem then forms: $R(\theta,\theta')\Phi(\theta',n) = \Lambda(n)\Phi(\theta,n)$ whose solution generates a discrete set of eigenvalues $\Lambda(n)$ with corresponding eigenvectors $\Phi(\theta,n)$ where n is an integer corresponding to the mode number ($n \in m$). Since eigenvectors are properties of the kernel, they can be used to reconstruct the variable space in two simple steps

$$a(t,n) = \sum_\theta p(\theta,t)\Phi(\theta,n) \tag{2}$$

$$\hat{p}^{(m)}(\theta,t) = \sum_n^m a(t,n)\Phi(\theta,n) \tag{3}$$

The reconstruction process is what allows certain signals to be retained while others are discarded (or filtered out). If ever a bias is introduced by the user, it occurs in the reconstruction process. If $m = \text{rank}(R_{\theta\theta'})$, then $\hat{p}^{(m)}(\theta,t) = p(\theta,t)$, and no filtering has been performed.

While POD can be used to decompose both variables, we will resort to Vold-Kalman filters (VKF) to decompose the other variables as this has the option of being performed in real time. In this case, a second generation Vold-Kalman multi-order tracking method is proposed.

5.3.2 *Vold-Kalman Multi-Order Tracking Filter*

Like POD, the VKF separates structure $P(\theta,t)$ from noise $\eta(\theta,t)$ using a two step reconstruction process as follows

$$s_k^\theta(t) = [H_{ttk}]^{-1}\Theta_k(t)^* p(\theta,t) \tag{4}$$

$$P(\theta,t) = \sum_k s_k^\theta(t)\Theta_k(t) \tag{5}$$

where $p(\theta,t) = P(\theta,t) + \eta(\theta,t)$ is the full signal, $s_k^\theta(t)$ is a low-frequency complex envelop, $\Theta_k(t)^*$ is a complex phasor, and the order of the filter k is denumerable. In practice, k defines the number of waveforms to be extracted. Similar to the role of the eigenvectors in the POD, the phasor serves to extract waveforms that make up the structured components of $p(\theta,t)$. The extraction is achieved by minimizing the error between the phasor and the raw signal and is performed using backward finite differencing. The crux of the problem is the formation of a multi-order difference matrix

$$[H_{ttk}]^{-1} = \begin{cases} r^2[A]^T[A] + [I], & \text{for} \quad k = l \\ \Theta_k(t)^*\Theta_l(t), & \text{for} \quad k \neq l \end{cases} \tag{6}$$

where r is a weighting parameter that depends on the number of poles in the filter, $[A]$ is a triangular array of coefficients and $[I]$ is an identity matrix. For a 2-pole filter, the weighting function is approximated numerically while the coefficients are based on Pascal's triangle and is written as

$$\begin{aligned} \nabla^2 s_k(t_i) &= s_k(t_{i+2}) - 2s_k(t_{i+1}) + s_k(t_i) \\ &= \epsilon(t_i) \end{aligned} \tag{7}$$

For a multi-order approach of order k, Eq. (7) resorts to an inverse problem of the form $[A][s_k^\theta(t)] = [\varepsilon_k(t)]$.

5.3.3 *Combining Methods*

There are several ways in which the POD and VKF techniques can be combined to dissect the different variables that make up the signal, thus making them complementary techniques. For the conventional POD, two options are proposed. The first uses VKF to filter the time variable by substituting $p(\theta,t)$ with its structured component $P(\theta,t)$ followed by a calculation of the POD coefficients. That is, Eqs. (4) and (5) are repeated for all of θ followed by the substitution of $P(\theta,t)$ into Eqs. (2) and (3) so that,

$$a_k(t,n) = \sum_\theta P(\theta,t)\Phi(\theta,n) \tag{8}$$

$$\hat{p}^{(mk)}(\theta,t) = \sum_n^m a_k(t,n)\Phi(\theta,n) \tag{9}$$

A potentially less costly alternative is to use the VKF to filter the POD coefficients $a(t,n)$ in place of the physical variable $p(\theta,t)$ since the opposing variable θ is suppressed during the summation process. In this case, the VKF is applied to individual POD expansion coefficients.

5.3.4 *Results*

In Fig. 8, normalized eigenvalues are shown for changes in rotor index angle where the denominator comprises the total resolved signal: $E = \sum_\theta \sum_t p(\theta,t)^2 = \sum_n \Lambda(n)$. The decay in convergence is less rapid as rotor index angle increases and advances from being dominated by two blade passes per rotation, to four blade-passes per rotation. As such, the sound field should be less structured and is an indicator of CDI rotor noise control.

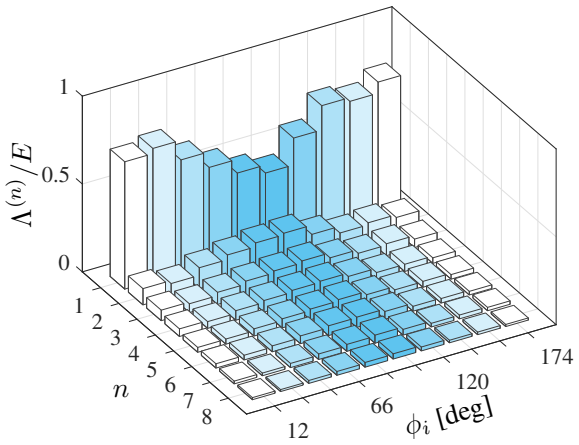

Figure 8. a) Normalized eigenvalue convergence and b) cumulative sum.

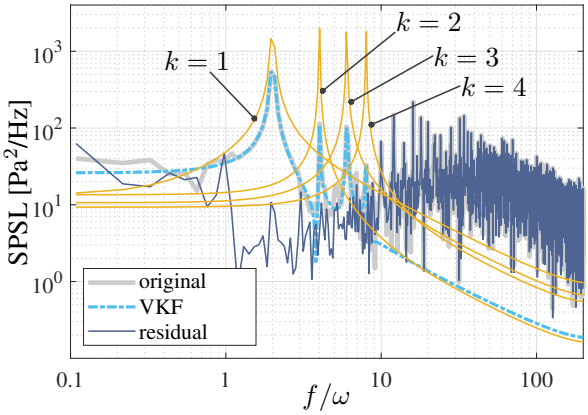

Figure 9. a) Sample acoustic time series with and without filtering, and b) its corresponding spectra superimposed the first four VKF phasors, the structural and residual components of the signal.

As for the VKF method, the instantaneous spectra of the raw acoustic pressure time series are shown in Fig. 9 superposed the structured component and its residual. Filtering is performed using $k = 4$ phasors corresponding to the first four blade pass frequency harmonics. Several reconstructions of the filtered sound field are then shown in Fig. 10 for changes to the rotor index angle and using the same combination of POD modes and VKF orders. When the upper and lower rotors are aligned and the sound field is a manifestation of constructive interference, sound waves are shown to extend over all observer positions. Eventually destructive interference takes over as the rotor index angle advances to a four blade configuration as seen in Figs. 10c and 10d.

5.4 Performance trade-space

An evaluation of the trade-space between rotor noise and hover performance is evaluated using Sound Pressure Levels (SPL) of the filtered waveforms at two observer locations in the far-field. The first is located at the rotor disk plane ($\theta = 0$ deg) while the second is where a ground observer would reside ($-\theta = 45$ deg). Symbol sizes increase with increasing index angle (ϕ). As seen in Fig. 11, rotor hover efficiency ranges from a maximum of 0.77 at $\varphi = -6$ deg, and then drops to 0.72 at $\varphi = 30$ deg. This change generates a 8% increase in hover performance with only a 0.40 dB and 0.03 dB increase in SPL for the rotor disk plane and ground observers, respectively. When implementing noise control measures through changes in rotor index angle, SPL levels drop by as much as 6 dB and 4 dB for the rotor disk plane and ground observers, respectively, while the rotor advances from $\varphi = -78$ deg to $\varphi = -6$ deg. This equates to a moderate loss in hover efficiency by -2%.

6. ACKNOWLEDGMENTS

Support for this effort was graciously provided through an internal research and development award with the Signal and Information Sciences Laboratory of the Applied Research Laboratories, The University of Texas at Austin.

7. REFERENCES

[1] C. E. Tinney and J. Valdez, "Thrust and acoustic performance of small-scale, coaxial, co-rotating rotors in hover," *AIAA Journal*, vol. 58, no. 4, pp. 1657–1667, 2020.

[2] C. E. Tinney, Y. Zhao-Dubuc, and J. Valdez, "The space-time structure of sound produced by stacked rotors in hover using vold-kalman filters and proper orthogonal decomposition," *Int. J. Aeroacoustics*, vol. 22, no. 5-6, pp. 576–598, 2023.

[3] J. Valdez and C. E. Tinney, "Wake of a coaxial, corotating rotor in hover," *AIAA Journal*, vol. 60, no. 8, pp. 4829–4839, 2022.

[4] C. E. Tinney and J. Valdez, "Higher-order statistical metrics for characterizing multirotor acoustics," *AIAA Journal*, vol. 62, no. 11, pp. 4431–4441, 2024.

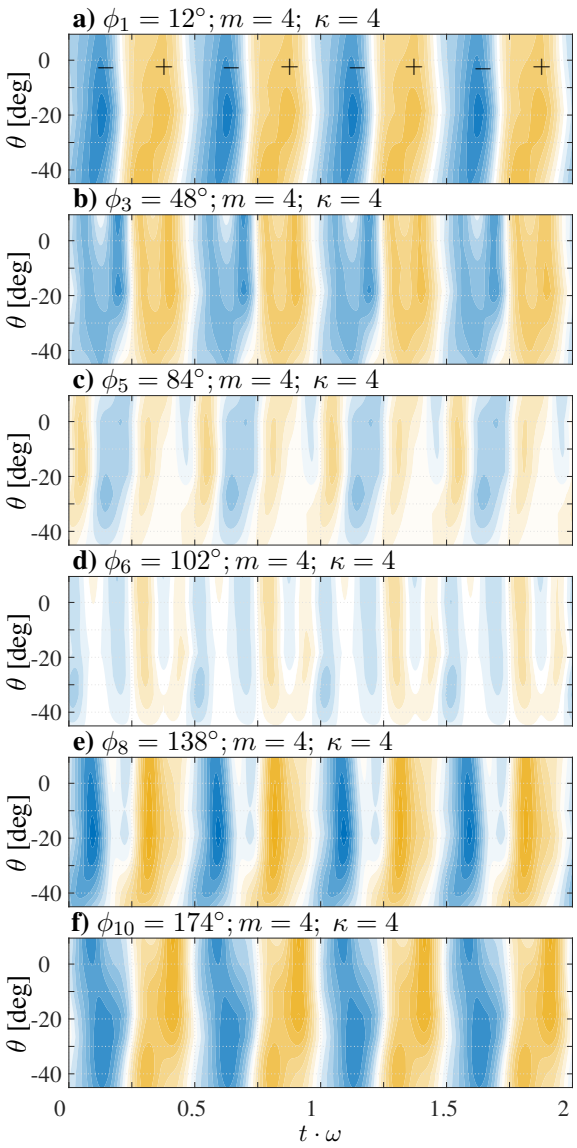

Figure 10. The sound field generated by the coaxial, corotating rotor for various index angles and filtered using $m = 4$ POD modes and $k = 4$ VKF phasors assigned to the first four blade pass frequency harmonics.

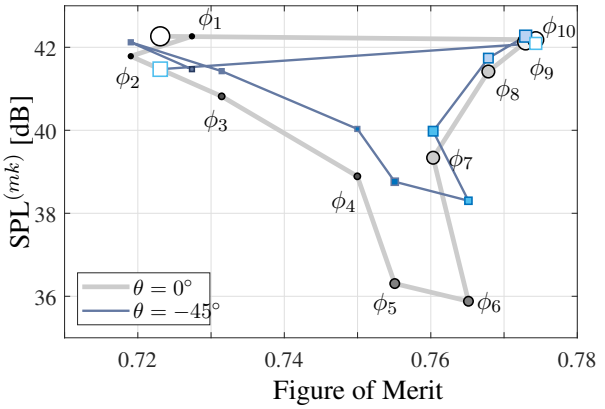

Figure 11. Trade space between filtered SPL and a) thrust coefficient, b) power coefficient, and c) rotor figure of merit.

[5] C. G. Cameron, A. Karpatne, and J. Sirohi, "Performance of a mach-scale coaxial counter-rotating rotor in hover," *Journal of Aircraft*, vol. 53, no. 3, pp. 746–755, 2016.

[6] E. Grande, S. Shubham, F. Avallone, and D. Ragni, "Computational aeroacoustic study of co-rotating rotors in hover," *Aerospace Science and Technology*, vol. 153, no. 109381, pp. 1–12, 2024.

[7] C. E. Tinney and J. Valdez, "Acoustic scaling for small rotors in hover," *Vertical Flight Society Forum 75, Paper 2019-14457*, 2019.

[8] C. E. Tinney and J. Valdez, "Hover performance and acoustics of a 35% scale notional evtol rotor," *AIAA Paper 2024-3219*, pp. 1–14, 2024.

[9] S. Mula, J. Stephenson, C. E. Tinney, and J. Sirohi, "Dynamical characteristics of the tip vortex from a four-bladed rotor in hover," *Experiments in Fluid*, vol. 54, no. 1600, 2013.

[10] D. Weitsman, J. H. Stephenson, and N. S. Zawodny, "Effects of flow recirculation on acoustic and dynamic measurements of rotary-wing systems operating in closed anechoic chambers," *Journal of the Acoustical Society of America*, vol. 148, no. 3, pp. 1325–1336, 2020.

[11] B. Henderson, D. Huff, J. Cluts, and C. Ruggeri, "Electric motor noise from small quadcopters: Part ii - source characteristics," *AIAA Paper 2018-2953*, pp. 1–23, 2018.

[12] C. E. Tinney and J. Sirohi, "Multirotor drone noise at static thrust," *AIAA Journal*, vol. 56, no. 7, pp. 2816–2826, 2018.